VALIDATION OF ACOUSTIC MODELS FOR TIME HARMONIC DISSIPATIVE SCATTERING PROBLEMS*

A. BERMÚDEZ[†], L. HERVELLA-NIETO[‡], A. PRIETO*[§], R. RODRÍGUEZ[¶]

Abstract

The aim of this paper is to study the time-harmonic scattering problem in a coupled fluid-porous medium system. We consider two different models for the treatment of porous materials: the Allard-Champoux equations and an approximate model based on a wall impedance condition. Both models are compared by computing analytically their respective solutions for unbounded planar obstacles, considering successively plane and spherical waves. A numerical method combining an optimal bounded PML and finite elements is also introduced to compute the solutions of both problems for more general axisymmetric geometries. This method is used to compare the solutions for a spherical absorber.

Keywords: Acoustic time-harmonic scattering problem; Porous medium; Allard-Champoux model; Wall impedance condition; Perfectly matched layer; Finite-element method.

1 Introduction

One of the most used techniques in passive control of noise consists of covering the reflecting surfaces with porous materials.

From a microscopic point of view, these materials consist of a solid skeleton, rigid or elastic, completely saturated by an acoustic fluid. This kind of absorbing materials are widely used because of its capability to dissipate acoustic waves, specially at low range frequencies.

*Available at http://dx.doi.org/10.1142/s0218396x07003238

[†]Departamento de Matemática Aplicada, Universidade de Santiago de Compostela, 15782 Santiago de Compostela, Spain mabermud@usc.es

[‡]Departamento de Matemáticas, Universidade da Coruña, 15707 A Coruña, Spain luisher@udc.es

[§]Departamento de Matemática Aplicada, Universidade de Santiago de Compostela, 15782 Santiago de Compostela, Spain andres.prieto@usc.es

[¶]GI^2MA, Departamento de Ingeniería Matemática, Universidad de Concepción, Casilla 160-C, Concepción, Chile rodolfo@ing-mat.udec.cl

There are several alternatives to derive models governing the vibrations of porous media; an overview can be found in Allard's book.[1]

If the solid skeleton is assumed to be rigid, the porous material can be considered as an equivalent fluid with dynamical density and bulk modulus coefficients depending on the frequency. These parameters can be obtained by empirical laws. In this setting, the equations introduced by Delany and Bazley[2] in 1970 have been widely used to describe sound propagation in fibrous materials. This model was subsequently improved by Morse and Ingard,[3] Attenborough,[4] and, more recently, by Allard and Champoux,[5] among others.

On the other hand, when the elastic deformation of the skeleton is taken into account, the theoretical basis for the mechanical behavior of the porous material was established by Biot.[6, 7] This theory describes the propagation of elastic waves in fluid-saturated porous media. The adaptation of this theory to acoustics can be found, for example, in the work of Allard *et al.*[8]

Furthermore, under the assumptions of rigid or elastic skeleton, it is also possible to obtain models for the motion of porous materials from a rigorous mathematical point of view by homogenization techniques.[9, 10]

The use of all these models can be inadequate when modeling the propagation of sound in an enclosure including porous media, since the thickness of the porous layer coating the reflecting surfaces is often much smaller than the characteristic dimensions of the physical domain of interest. This difference in size is typically a serious drawback to create a mesh of the domain in order to compute the acoustic field with, for instance, a finite-element method.

If we assume that the porous layers are thin, this numerical difficulty can be overcome by substituting the partial differential equations governing the porous medium by a wall impedance condition on the coated boundaries. This boundary condition involves frequency dependent coefficients which can be theoretically computed from the dynamic density and bulk modulus of the coating porous material in the case of incident plane waves on a plane surface (see Section 2.3 below). Let us remark that the two models do not necessarily lead to the same solution for more general geometric conditions.

We compare in this paper a fluid-porous model with an approximation obtained by replacing the porous media by a wall impedance condition. We study the dependence of both models with respect to the thickness of the porous layer, the frequency, the acoustic source and the geometry of the problem domain. More precisely, we study the accuracy of the wall impedance model versus the Allard-Champoux model for time-harmonic scattering problems in unbounded three-dimensional domains. Many problems with practical interest fall in this framework, as for instance the numerical simulation of real experiments involving absorbing materials in an anechoic or semi-anechoic room.[11]

The fluid-porous scattering problems can be solved analytically only for some geometrically simple domains. However, in general, it is necessary to use numerical techniques. Because of its easy implementation and its effectiveness in handling complex geometries, the finite-element method has become popular to solve such problems. Some examples of the finite element method applied to sound propagation in porous media are the papers by Easwaran *et al.*,[12]

Panneton and Atalla,[13] and Bermúdez *et al.*[14] All of them consider acoustic propagation inside rigid cavities and, hence, the problems are posed in bounded domains.

For problems posed on unbounded domains, finite-element methods require first to truncate the computational domain without perturbing too much the solution of the original problem. Several techniques are available to do this: absorbing boundary conditions,[15] boundary elements,[16] infinite elements,[17] etc. In the present paper, we will use the so called PML (*Perfectly Matched Layer*) method, introduced by Berenger.[18]

The PML method is based on simulating an absorbing layer of damping material surrounding the domain of interest, like a thin sponge which absorbs the scattered field radiated to the exterior of this domain. This method is known as 'perfectly matched' because the interface between the physical domain and the absorbing layer does not produce spurious reflections.

In practice, since the PML has to be truncated at a finite distance of the domain of interest, its external boundary produces artificial reflections. Theoretically, these reflections are of minor importance because of the exponential decay of the acoustic waves inside the PML, but the approximation error typically becomes larger once the problem is discretized. Increasing the thickness of the PML may be a remedy, although not always available because of its computational cost. An alternative usual choice to achieve low error levels is to take larger values of the absorption coefficients in the layer. However, Collino and Monk[19] showed that this methodology may produce an increasing error in the discretized problem.

We will use an alternative procedure to avoid this numerical drawback, which we have proposed and analyzed in a previous paper.[20] It consists of using an absorbing function with unbounded integral on the PML. In such case, the exact solution of the original time-harmonic scattering problem in the domain of interest is recovered, even though the thickness of the layer is finite.

The outline of this paper is as follows: In Section 2 we state the scattering problems in a three-dimensional unbounded domain with a porous layer surrounding a rigid obstacle. We introduce the Allard-Champoux equations, governing the motion in the porous layer, and the wall impedance model. Then we compute the frequency dependent impedance which yields the equivalence between both models under the assumption of plane waves with normal incidence. In Section 3, we study the particular case where the obstacle is planar and unbounded. For this simple geometry we obtain the exact solution for the scattering problem assuming plane waves of oblique incidence or spherical waves. In both cases we compare the pressure fields computed from the two models. In Section 4, under the hypothesis of spherical geometry, both models are numerically solved by using an optimal bounded PML technique combined with a finite-element method. Finally, we report the numerical results obtained with this approach, when the obstacle is a sphere covered by a porous material.

2 Statement of the problem. Mathematical modeling

We consider in this section a time-harmonic scattering problem for a coupled system formed by an acoustic fluid and a porous medium.

Let Ω be a domain (bounded or unbounded) occupied by an obstacle to the propagation of acoustic waves, with a totally reflecting boundary Γ and outward unit normal vector $\boldsymbol{\nu}$. We consider a set of coordinates with its origin lying inside the obstacle.

Let Ω_{A} be another domain surrounding the obstacle and occupied by a porous material, with outer boundary Γ_{I} and outward normal unit vector $\boldsymbol{n}$. The rest of the space, Ω_{F}, is filled with an acoustic fluid (i.e., compressible, barotropic and inviscid). Fig. 1 shows a two-dimensional section of the domains.

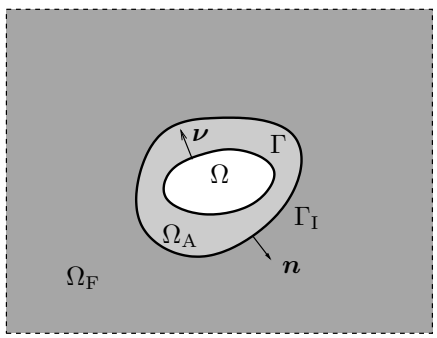

Figure 1: Two-dimensional vertical section of the domains.

In what follows we introduce the equations of the time-harmonic scattering problem with two different models for the porous medium.

2.1 The Allard-Champoux model

The first model consists of using directly the Allard-Champoux equations governing the porous material. Consider a periodic acoustic source with angular frequency ω and amplitude F acting inside Ω_{F}. The amplitudes of the pressure fields in Ω_{F} and Ω_{A} are, respectively, the solutions P_1 and P_{A} of the following

equations:

$$\frac{1}{\rho_{\mathrm{F}}}\Delta P_1 + \frac{\omega^2}{\mu_{\mathrm{F}}} P_1 = F \qquad \text{in } \Omega_{\mathrm{F}}, \tag{1}$$

$$\frac{1}{\rho_{\mathrm{A}}}\Delta P_{\mathrm{A}} + \frac{\omega^2}{\mu_{\mathrm{A}}} P_{\mathrm{A}} = 0 \qquad \text{in } \Omega_{\mathrm{A}}, \tag{2}$$

$$P_1 = P_{\mathrm{A}} \qquad \text{on } \Gamma_{\mathrm{I}}, \tag{3}$$

$$\frac{1}{\rho_{\mathrm{F}}}\frac{\partial P_1}{\partial \boldsymbol{n}} = \frac{1}{\rho_{\mathrm{A}}}\frac{\partial P_{\mathrm{A}}}{\partial \boldsymbol{n}} \qquad \text{on } \Gamma_{\mathrm{I}}, \tag{4}$$

$$\frac{1}{\rho_{\mathrm{A}}}\frac{\partial P_{\mathrm{A}}}{\partial \boldsymbol{\nu}} = 0 \qquad \text{on } \Gamma, \tag{5}$$

$$\lim_{r\to+\infty} r\left(\frac{1}{ik_{\mathrm{F}}}\frac{\partial P_1}{\partial r} - P_1\right) = 0 \qquad \text{in } \Omega_{\mathrm{F}}, \tag{6}$$

$$\lim_{r\to+\infty} r\left(\frac{1}{ik_{\mathrm{A}}}\frac{\partial P_{\mathrm{A}}}{\partial r} - P_{\mathrm{A}}\right) = 0 \qquad \text{in } \Omega_{\mathrm{A}}. \tag{7}$$

Eq. (1) is the standard Helmholtz equation for an acoustic fluid, where ρ_{F} is the mass density of the fluid at rest and μ_{F} its bulk modulus which, for an acoustic fluid, is given by $\mu_{\mathrm{F}} = \rho_{\mathrm{F}} c_{\mathrm{F}}^2$, with c_{F} being the sound speed in the fluid.

Eq. (2) corresponds to the Allard-Champoux[5] model for the vibrations in Ω_{A}. This model assumes that the skeleton of the porous medium is rigid. In fact, it considers that the medium consists of a fluid-saturated rigid fibrous material. It also assumes that the thermal exchange between the fluid and the fibers of the porous medium is not negligible. If the porous material is assumed to be isotropic from a macroscopic point of view, then the pressure in the porous medium satisfies Eq. (2), where ρ_{A} and μ_{A} are the so called dynamic density and dynamic bulk modulus, respectively, which depend on the frequency. These coefficients are given by the following expressions:

$$\mu_{\mathrm{A}} = \mu_{\mathrm{A}}(\omega) = \gamma P_0 \left[\gamma - \frac{\gamma - 1}{1 + \dfrac{i}{4\mathrm{Pr}}\dfrac{\sigma}{\rho_{\mathrm{F}}\omega} G_2\left(\dfrac{\rho_{\mathrm{F}}\omega}{\sigma}\right)}\right]^{-1},$$

$$\rho_{\mathrm{A}} = \rho_{\mathrm{A}}(\omega) = \rho_{\mathrm{F}}\left[1 + i\left(\frac{\sigma}{\rho_{\mathrm{F}}\omega}\right) G_1\left(\frac{\rho_{\mathrm{F}}\omega}{\sigma}\right)\right].$$

In the above empirical equations, P_0 is the fluid equilibrium pressure at rest, γ the ratio of specific heats of the fluid, Pr the Prandtl number and σ the flow resistivity. Finally, functions G_1 and G_2 are given by

$$G_1\left(\frac{\rho_{\mathrm{F}}\omega}{\sigma}\right) = \sqrt{1 - \frac{i}{2}\frac{\rho_{\mathrm{F}}\omega}{\sigma}} \qquad \text{and} \qquad G_2\left(\frac{\rho_{\mathrm{F}}\omega}{\sigma}\right) = G_1\left(4\mathrm{Pr}\frac{\rho_{\mathrm{F}}\omega}{\sigma}\right).$$

Eq. (3) and (4) are the usual kinematic and kinetic interface conditions, which preserve continuity of pressure and velocity fields, respectively, whereas

Eq. (5) is the standard reflecting condition on a rigid obstacle. Finally, Eq. (6) and (7) are the radiation Sommerfeld conditions in fluid and porous domains, with k_{F} and k_{A} being the respective wave numbers

$$k_{\mathrm{F}} = \omega\sqrt{\frac{\rho_{\mathrm{F}}}{\mu_{\mathrm{F}}}} = \frac{\omega}{c_{\mathrm{F}}} \qquad \text{and} \qquad k_{\mathrm{A}} = \omega\sqrt{\frac{\rho_{\mathrm{A}}}{\mu_{\mathrm{A}}}}. \tag{8}$$

Let us remark that Eq. (7) only holds if the porous medium domain is unbounded.

2.2 The wall impedance model

An alternative to model the effect of the porous medium, valid in principle when the thickness of the porous layer is negligible, consists of replacing the equation in Ω_{A} by a complex-valued frequency-dependent wall impedance condition on Γ_{I}. This condition is defined as to recover the exact pressure field in problems involving plane waves with normal incidence, as will be shown in the next subsection.

Consider again the notation shown in Fig. 1 and the same periodic acoustic source as above. The amplitude of the pressure field in Ω_{F} is now the solution P_2 of the following exterior Helmholtz problem:

$$\frac{1}{\rho_{\mathrm{F}}}\Delta P_2 + \frac{\omega^2}{\mu_{\mathrm{F}}}P_2 = F \qquad \text{in } \Omega_{\mathrm{F}}, \tag{9}$$

$$P_2 - \frac{Z}{i\omega\rho_{\mathrm{F}}}\frac{\partial P_2}{\partial \boldsymbol{n}} = 0 \qquad \text{on } \Gamma_{\mathrm{I}}, \tag{10}$$

$$\lim_{r\to+\infty} r\left(\frac{1}{ik_{\mathrm{F}}}\frac{\partial P_2}{\partial r} - P_2\right) = 0 \qquad \text{in } \Omega_{\mathrm{F}}. \tag{11}$$

Eq. (10) is the wall impedance condition which models the layer of porous material covering the obstacle and involves the frequency-dependent wall impedance coefficient Z. Since the fluid is assumed to be inviscid, this condition only involves the normal derivative of the pressure.

2.3 Computing the wall impedance

In what follows we compute the complex frequency-dependent wall impedance coefficient Z, in such a way that the solutions P_1 and P_2 of problems (1)-(7) and (9)-(11), respectively, coincide under the assumption of plane waves with normal incidence. Let us recall that this is the standard assumption for a Kundt's tube.

Consider fluid and porous medium domains, Ω_{F} and Ω_{A}, respectively, as in Fig. 2. Assume that the source term is now a plane wave with normal incidence to Γ_{I} with amplitude P_{inc}. Assume also that this plane wave has a zero phase on the plane $x_3 = a$. We introduce this source in both problems through the following boundary condition:

$$-\frac{1}{2}\left(\frac{1}{ik_{\mathrm{F}}}\frac{\partial P_j}{\partial x_3} - P_j\right)\bigg|_{x_3=a} = P_{\mathrm{inc}}, \qquad j = 1, 2.$$

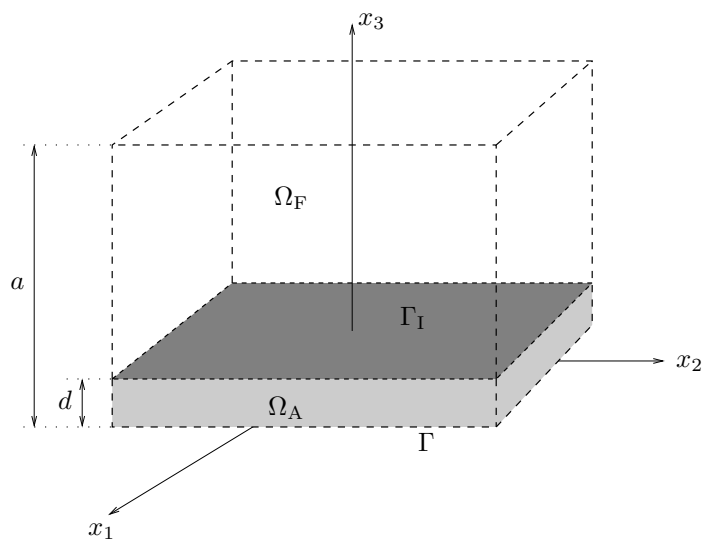

Figure 2: Unbounded obstacle with planar boundary. 3D domains.

It is clear that with this boundary condition and without any other source term in the fluid domain, the solution is composed of different plane waves with normal incidence.

Eq. (1)-(7) reduce in this case to the following one-dimensional problem:

$$\begin{cases} \dfrac{1}{\rho_{\mathrm{F}}}\dfrac{d^2P_1}{dx_3^2}+\dfrac{\omega^2}{\mu_{\mathrm{F}}}P_1=0, & d<x_3<a,\\ \dfrac{1}{\rho_{\mathrm{A}}}\dfrac{d^2P_{\mathrm{A}}}{dx_3^2}+\dfrac{\omega^2}{\mu_{\mathrm{A}}}P_{\mathrm{A}}=0, & 0>x_3>d,\\ -\dfrac{1}{2}\left(\dfrac{1}{ik_{\mathrm{F}}}\dfrac{dP_1}{dx_3}-P_1\right)=P_{\mathrm{inc}}, & x_3=a,\\ P_1=P_{\mathrm{A}} & x_3=d,\\ \dfrac{1}{\rho_{\mathrm{F}}}\dfrac{dP_1}{dx_3}=\dfrac{1}{\rho_{\mathrm{A}}}\dfrac{dP_{\mathrm{A}}}{dx_3}, & x_3=d,\\ \dfrac{1}{\rho_{\mathrm{A}}}\dfrac{dP_{\mathrm{A}}}{dx_3}=0, & x_3=0. \end{cases} \tag{12}$$

Straightforward computations lead to

$$P_1(x_1,x_2,x_3)=P_{\mathrm{inc}}\left[\mathrm{e}^{-ik_{\mathrm{F}}(x_3-a)}+R_1\,\mathrm{e}^{ik_{\mathrm{F}}(x_3+a)}\right],$$

where the reflection coefficient R_1 is given by

$$R_1=\mathrm{e}^{-2ik_{\mathrm{F}}d}\,\frac{Z_{\mathrm{A}}\cos(k_{\mathrm{A}}d)+iZ_{\mathrm{F}}\sin(k_{\mathrm{A}}d)}{Z_{\mathrm{A}}\cos(k_{\mathrm{A}}d)-iZ_{\mathrm{F}}\sin(k_{\mathrm{A}}d)},$$

with

$$Z_{\mathrm{F}} = \frac{\omega\rho_{\mathrm{F}}}{k_{\mathrm{F}}} = \rho_{\mathrm{F}} c_{\mathrm{F}} \qquad \text{and} \qquad Z_{\mathrm{A}} = \frac{\omega\rho_{\mathrm{A}}}{k_{\mathrm{A}}}$$

being the characteristic impedances of the fluid and the porous medium, respectively.

Analogously, Eq. (9)-(11) yield in this case the following one-dimensional problem:

$$\begin{cases} \dfrac{1}{\rho_{\mathrm{F}}}\dfrac{d^2P_2}{dx_3^2} + \dfrac{\omega^2}{\mu_{\mathrm{F}}}P_2 = 0, & d < x_3 < a, \\ -\dfrac{1}{2}\left(\dfrac{1}{ik_{\mathrm{F}}}\dfrac{dP_2}{dx_3} - P_2\right) = P_{\mathrm{inc}}, & x_3 = a, \\ P_2 - \dfrac{Z}{i\omega\rho_{\mathrm{F}}}\dfrac{dP_2}{dx_3} = 0, & x_3 = d. \end{cases} \tag{13}$$

In this case, it is simple to show that

$$P_2(x_1, x_2, x_3) = P_{\mathrm{inc}}\left[\mathrm{e}^{-ik_{\mathrm{F}}(x_3-a)} + R_2\,\mathrm{e}^{ik_{\mathrm{F}}(x_3+a)}\right],$$

with

$$R_2 = \mathrm{e}^{-2ik_{\mathrm{F}}d}\,\frac{Z + Z_{\mathrm{F}}}{Z - Z_{\mathrm{F}}}.$$

Thus, it is possible to define a particular complex-valued coefficient Z so that its solution coincides with that of problem (12). Thus we obtain the following result:

Proposition 2.1. *Let P_1 and P_2 be the solutions of problems (12) and (13), respectively. If*

$$Z = Z_{\mathrm{A}}\coth(ik_{\mathrm{A}}d), \tag{14}$$

then $P_1(x_1, x_2, x_3) = P_2(x_1, x_2, x_3)$, for $d < x_3 < a$.

This is a classical result.[22] Eq. (14) is nothing but the well-known expression of the input impedance to a rigidly backed porous layer with thickness d.

3 Planar unbounded wall

In this section we will deal with other particular problems in which the obstacle and the absorbing layer are unbounded and have a planar boundary as in Fig. 2. We will consider two simple source terms: plane waves with oblique incidence and spherical waves. In both cases, we will deduce explicit formulas for the solutions of problems (1)-(7) and (9)-(11), which will allow us to compare both models.

In spite of the fact that the assumption of an unbounded absorbing layer is not realistic, it allows us to avoid the diffraction effects due to the borders of the porous sample. This assumption is usually made, even from an experimental point of view, when the size of the sample is much larger than the length wave of the acoustic source.

3.1 Plane waves with oblique incidence

Consider now as a source term a plane wave of amplitude $P_{\rm inc}$ with oblique incidence on the interface $\Gamma_{\rm I}$, the incidence angle being α. We assume again that this plane wave has a zero phase with respect to the variable x_3 on the plane $x_3 = a$, so that we introduce the source term by means of the following boundary condition:

$$-\frac{1}{2}\left(\frac{1}{ik_{\rm F}\cos\alpha}\frac{\partial P_j}{\partial x_3} - P_j\right)\bigg|_{x_3=a} = P_{\rm inc}\,{\rm e}^{-ik_{\rm F}x_2\sin\alpha}, \qquad j = 1, 2.$$

In this case, Eq. (1)-(7) reduce to the following two-dimensional problem:

$$\left\{\begin{array}{rl}
\dfrac{1}{\rho_{\rm F}}\dfrac{\partial^2 P_1}{\partial x_2^2} + \dfrac{1}{\rho_{\rm F}}\dfrac{\partial^2 P_1}{\partial x_3^2} + \dfrac{\omega^2}{\mu_{\rm F}}P_1 = 0, & d < x_3 < a,\\[2ex]
\dfrac{1}{\rho_{\rm A}}\dfrac{\partial^2 P_{\rm A}}{\partial x_2^2} + \dfrac{1}{\rho_{\rm A}}\dfrac{\partial^2 P_{\rm A}}{\partial x_3^2} + \dfrac{\omega^2}{\mu_{\rm A}}P_{\rm A} = 0, & 0 < x_3 < d,\\[2ex]
-\dfrac{1}{2}\left(\dfrac{1}{ik_{\rm F}\cos\alpha}\dfrac{\partial P_1}{\partial x_3} - P_1\right) = P_{\rm inc}\,{\rm e}^{-ik_{\rm F}x_2\sin\alpha}, & x_3 = a,\\[2ex]
P_1 = P_{\rm A}, & x_3 = d,\\[2ex]
\dfrac{1}{\rho_{\rm F}}\dfrac{\partial P_1}{\partial x_3} = \dfrac{1}{\rho_{\rm A}}\dfrac{\partial P_{\rm A}}{\partial x_3}, & x_3 = d,\\[2ex]
\dfrac{1}{\rho_{\rm A}}\dfrac{\partial P_{\rm A}}{\partial x_3} = 0, & x_3 = 0.
\end{array}\right. \tag{15}$$

Straightforward computations lead now to the following expression for P_1:

$$P_1(x_1, x_2, x_3) = P_{\rm inc}\,{\rm e}^{-ik_{\rm F}x_2\sin\alpha}\left[{\rm e}^{-ik_{\rm F}(x_3-a)\cos\alpha} + R_1\,{\rm e}^{ik_{\rm F}(x_3+a)\cos\alpha}\right], \tag{16}$$

where the reflection coefficient R_1, which depends on the frequency and the incidence angle, is given by

$$R_1 = {\rm e}^{-2ik_{\rm F}d\cos\alpha}\,\frac{Z_{\rm A}^*\cos\alpha\,\cos(k_{\rm A}^* d) + iZ_{\rm F}\sin(k_{\rm A}^* d)}{Z_{\rm A}^*\cos\alpha\,\cos(k_{\rm A}^* d) - iZ_{\rm F}\sin(k_{\rm A}^* d)},$$

with

$$k_{\rm A}^* = \sqrt{k_{\rm A}^2 - k_{\rm F}^2\sin^2\alpha} \qquad \text{and} \qquad Z_{\rm A}^* = \omega\rho_{\rm A}/k_{\rm A}^*,$$

whereas $Z_{\rm F} = \omega\rho_{\rm F}/k_{\rm F} = \rho_{\rm F}c_{\rm F}$, as above.

Analogously, under the assumption of plane waves with oblique incidence, problem (9)-(11) can be written as follows:

$$\left\{\begin{array}{rl}
\dfrac{1}{\rho_{\rm F}}\dfrac{\partial^2 P_2}{\partial x_2^2} + \dfrac{1}{\rho_{\rm F}}\dfrac{\partial^2 P_2}{\partial x_3^2} + \dfrac{\omega^2}{\mu_{\rm F}}P_2 = 0, & d < x_3 < a,\\[2ex]
-\dfrac{1}{2}\left(\dfrac{1}{ik_{\rm F}\cos\alpha}\dfrac{\partial P_2}{\partial x_3} - P_2\right) = P_{\rm inc}\,{\rm e}^{-ik_{\rm F}x_2\sin\alpha}, & x_3 = a,\\[2ex]
P_2 - \dfrac{Z}{i\omega\rho_{\rm F}}\dfrac{\partial P_2}{\partial x_3} = 0, & x_3 = d.
\end{array}\right. \tag{17}$$

Proceeding as above, it is easy to show that the pressure field is given by

$$P_2(x_1, x_2, x_3) = P_{\rm inc}\, {\rm e}^{-ik_{\rm F} x_2 \sin\alpha} \left[{\rm e}^{-ik_{\rm F}(x_3-a)\cos\alpha} + R_2\, {\rm e}^{ik_{\rm F}(x_3+a)\cos\alpha} \right], \quad (18)$$

where the reflection coefficient is now

$$R_2 = {\rm e}^{-2ik_{\rm F} d \cos\alpha}\, \frac{Z\cos\alpha + Z_{\rm F}}{Z\cos\alpha - Z_{\rm F}}.$$

The expression of the input impedance for plane waves with oblique incidence in a multilayered media is also well known.[22] In principle, we could use it to define Z so that we recover the equivalence between the solutions of problems (15) and (17). However, this value of Z would depend on the incidence angle α.

Our aim is to characterize the behavior of a porous layer by a wall impedance depending only on the thickness and the physical properties of the porous material, but not on the particular acoustic source. Because of this, we propose to use the wall impedance (14) computed for plane waves with normal incidence. In what follows, we compare the solutions (16) and (18) of problems (15) and (17), respectively, as a first validation of this proposal.

For the fluid parameters we have used $\rho_{\rm F} = 1.2\,{\rm kg/m^3}$ and $c_{\rm F} = 343\,{\rm m/s}$, whereas, for the porous layer, ${\rm Pr} = 0.702$, $\gamma = 1.4$, $\sigma = 20000$ rays mks and $P_0 = 101320\,{\rm N/m^2}$, the thickness of the layer being $d = 0.05\,{\rm m}$.

Fig. 3 shows the real and the imaginary parts of the wall impedance defined in (14) for a range of frequencies $f = \omega/(2\pi)$ between 100 and 2000 Hz.

We consider an incoming plane wave of oblique incidence with angle $\alpha = \pi/3\,{\rm rad}$, amplitude $P_{\rm inc} = 1\,{\rm N/m^2}$ and null x_3-phase on the plane $x_3 = 1\,{\rm m}$.

As a first test, we compute the solutions P_1 and P_2 provided by each model at different observation points on the x_3-axis that we call $\boldsymbol{m}_1$, $\boldsymbol{m}_2$, $\boldsymbol{m}_3$ and $\boldsymbol{m}_4$ (see Fig. 4), for a wide range of frequencies.

We show the real parts of the results in Fig. 5, where the agreement of both models can be clearly appreciated. Indeed, the agreement is so good that, for each of the observation points, the curves corresponding to each model almost coincide, making it very hard to distinguish one from the other.

For plane waves, there is no need of comparing the solution provided by both models at points with the same coordinate z, as $\boldsymbol{m}_5, \ldots, \boldsymbol{m}_8$ in Fig. 4. Indeed, $P_1(\boldsymbol{m}_j)$, $j = 4, \ldots, 8$, only differ in phase, and the same happens with $P_2(\boldsymbol{m}_j)$ (see Eq. (16) and (18)). Clearly, this is not the case for more general waves as will be shown in the next section.

Finally, we check the agreement between both models for different values of the thickness of the porous material. In Fig. 6 we show the relative difference between both solutions, $|P_1 - P_2| \,/\, |P_{\rm inc}|$, at the points $\boldsymbol{m}_1$ and $\boldsymbol{m}_4$ (see Fig. 4), for a couple of frequencies and a wide range of values of the thickness.

We observe that the agreement between both models is essentially independent of the point where we compute the pressure field. Moreover, the relative difference between both models does not increase with frequency. On the other

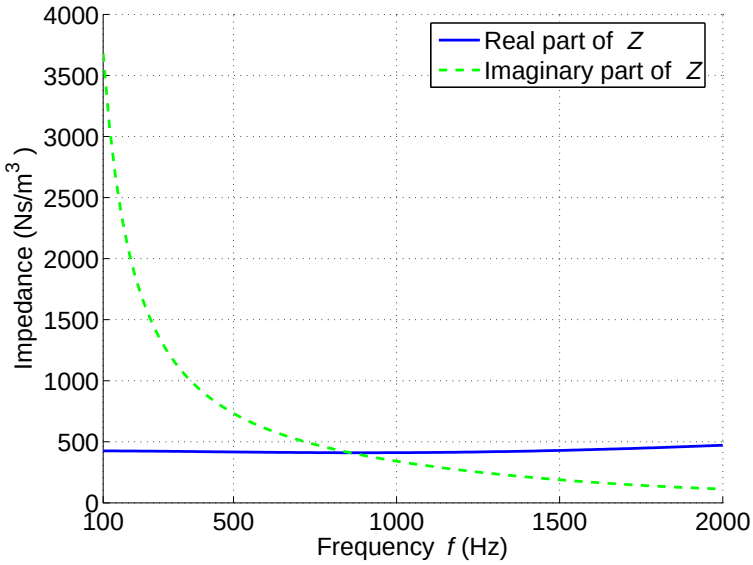

Figure 3: Wall impedance Z as defined by Eq. (14) for different values of $f = \omega/(2\pi)$.

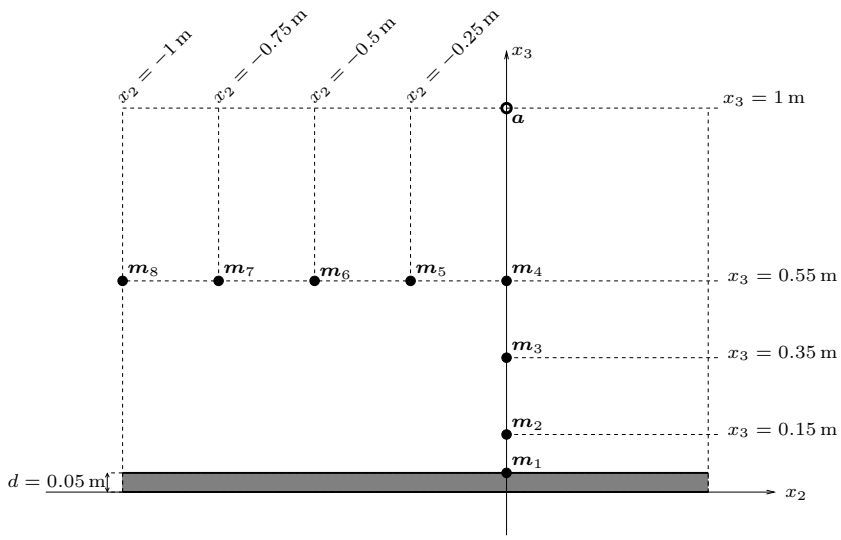

Figure 4: Observation points for the pressure field.

hand, even for a thick porous layer and moderate values of the angle of incidence ($\alpha = \pi/3\,\mathrm{rad}$), the agreement does not degenerate. Indeed each curve shows only one small error peak for very small values of the thickness d ($\approx 12\%$

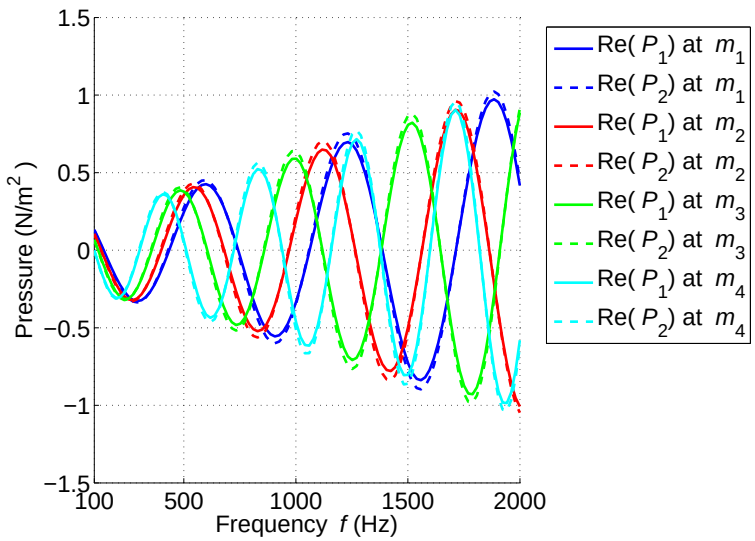

Figure 5: Plane waves with oblique incidence. Real part of the pressure fields at different points.

for 1000 Hz and $\approx 6\%$ for 500 Hz).

3.2 Spherical waves

Next we consider a new source term: a monopole acting inside the fluid domain. In this case, the technique to obtain the solutions of the scattering problems is classical.[23] For completeness, we detail the computations for the Allard-Champoux model.

For a monopole at the point $\boldsymbol{a} = (0, 0, a)$, with constant volume velocity Q,[18] the acoustic source term in (1) is $F = i\omega Q \delta_{\boldsymbol{a}}$, with $\delta_{\boldsymbol{a}}$ being the Dirac's delta with support at $\boldsymbol{a}$.

Since the source term depends neither on x_1 nor on x_2, and the interfaces Γ_{I} and Γ are orthogonal to the x_3-axis, we take advantage of the symmetry of the problem. We use the two-dimensional Fourier transform[24] in the space variables x_1 and x_2:

$$\widehat{P}_1(\widehat{x}_1, \widehat{x}_2, x_3) = \int_{-\infty}^{+\infty} \int_{-\infty}^{+\infty} P_1(x_1, x_2, x_3)\, \mathrm{e}^{-i\widehat{x}_1 x_1}\, \mathrm{e}^{-i\widehat{x}_2 x_2}\, dx_1\, dx_2.$$

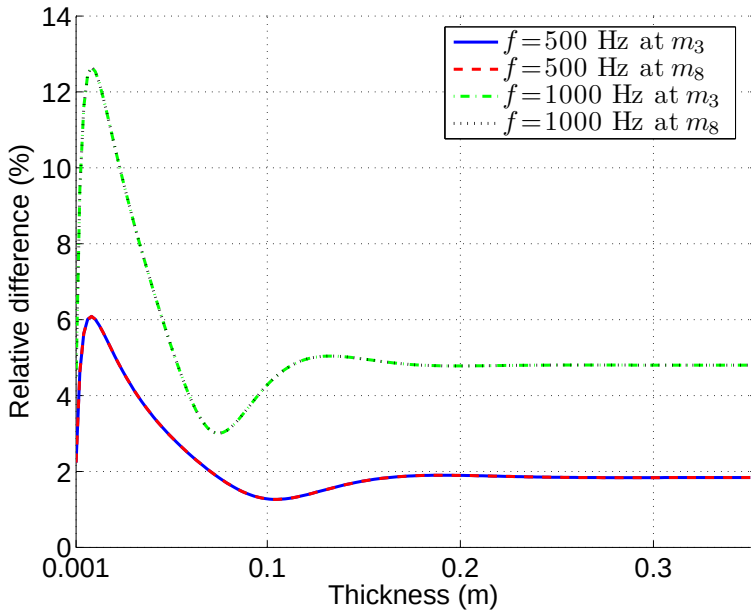

Figure 6: Plane waves with oblique incidence. $|P_1 - P_2| \,/\, |P_{\rm inc}|$ versus thickness of the porous layer.

Taking Fourier transform of Eq. (1) and (2), we obtain:

$$\begin{cases} \dfrac{1}{\rho_{\rm F}}\left[-(\widehat{x}_1^2+\widehat{x}_2^2)\widehat{P}_1 + \dfrac{\partial^2 \widehat{P}_1}{\partial x_3^2}\right] + \omega^2 \dfrac{1}{\mu_{\rm F}}\widehat{P}_1 = i\omega Q \widehat{\delta}_{\boldsymbol{a}} & \text{in } \Omega_{\rm F}, \\ \dfrac{1}{\rho_{\rm A}}\left[-(\widehat{x}_1^2+\widehat{x}_2^2)\widehat{P}_{\rm A} + \dfrac{\partial^2 \widehat{P}_{\rm A}}{\partial x_3^2}\right] + \omega^2 \dfrac{1}{\mu_{\rm A}}\widehat{P}_{\rm A} = 0 & \text{in } \Omega_{\rm A}. \end{cases}$$

Notice that $\widehat{\delta}_{\boldsymbol{a}}$ coincides with the one-variable Dirac's delta with support at the point $x_3 = a$. Hence, by using the Sommerfeld radiation conditions (6) and (7), we obtain:

$$\widehat{P}_1(\widehat{x}_1, \widehat{x}_2, x_3) = \frac{\omega \rho_{\rm F} Q \, {\rm e}^{i\sqrt{k_{\rm F}^2 - \widehat{r}^2}\,|x_3 - a|}}{2\sqrt{k_{\rm F}^2 - \widehat{r}^2}} + \widehat{R}_1 \, {\rm e}^{i\sqrt{k_{\rm F}^2 - \widehat{r}^2}\, x_3}, \tag{19}$$

$$\widehat{P}_{\rm A}(\widehat{x}_1, \widehat{x}_2, x_3) = T_{\rm A} \, {\rm e}^{-i\sqrt{k_{\rm A}^2 - \widehat{r}^2}\, x_3} + R_{\rm A} \, {\rm e}^{i\sqrt{k_{\rm A}^2 - \widehat{r}^2}\, x_3}, \tag{20}$$

where $\widehat{r} = \sqrt{\widehat{x}_1^2 + \widehat{x}_2^2}$, and $k_{\rm F}$ and $k_{\rm A}$ are the wave numbers in the fluid and in the porous media, respectively, as defined in (8).

We introduce the following notation:

$$\widehat{k}_{\rm F} = \sqrt{k_{\rm F}^2 - \widehat{r}^2}, \qquad \widehat{k}_{\rm A} = \sqrt{k_{\rm A}^2 - \widehat{r}^2}, \qquad \widehat{Z}_{\rm F} = \frac{\omega \rho_{\rm F}}{\widehat{k}_{\rm F}}, \qquad \widehat{Z}_{\rm A} = \frac{\omega \rho_{\rm A}}{\widehat{k}_{\rm A}}.$$

The interface conditions (3)-(5) lead to the following system of equations for the coefficients R_{A}, $\widehat{R}_1$ and T_{A}:

$$\left\{\begin{array}{rcl} \dfrac{\widehat{Z}_{\mathrm{F}}Q}{2}\,\mathrm{e}^{i\widehat{k}_{\mathrm{F}}(d-a)} + \widehat{R}_1\,\mathrm{e}^{i\widehat{k}_{\mathrm{F}}d} & = & T_{\mathrm{A}}\,\mathrm{e}^{-i\widehat{k}_{\mathrm{A}}d} + R_{\mathrm{A}}\,\mathrm{e}^{i\widehat{k}_{\mathrm{A}}d}, \\ -\dfrac{Q}{2}\,\mathrm{e}^{i\widehat{k}_{\mathrm{F}}(d-a)} + \dfrac{\widehat{R}_1}{\widehat{Z}_{\mathrm{F}}}\,\mathrm{e}^{i\widehat{k}_{\mathrm{F}}d} & = & -\dfrac{T_{\mathrm{A}}}{\widehat{Z}_{\mathrm{A}}}\,\mathrm{e}^{-i\widehat{k}_{\mathrm{A}}d} + \dfrac{R_{\mathrm{A}}}{\widehat{Z}_{\mathrm{A}}}\,\mathrm{e}^{i\widehat{k}_{\mathrm{A}}d}, \\ -T_{\mathrm{A}} + R_{\mathrm{A}} & = & 0. \end{array}\right.$$

Notice that since $\widehat{k}_{\mathrm{F}}$ and $\widehat{k}_{\mathrm{A}}$ depend on $\widehat{x}_1$ and $\widehat{x}_2$ through $\widehat{r}$, so do R_{A}, $\widehat{R}_1$ and T_{A}.

By solving this linear system, we obtain

$$\widehat{R}_1 = \mathrm{e}^{-2i\widehat{k}_{\mathrm{F}}d}\,\frac{\widehat{Z}_{\mathrm{A}}\cos(\widehat{k}_{\mathrm{A}}d) + i\widehat{Z}_{\mathrm{F}}\sin(\widehat{k}_{\mathrm{A}}d)}{\widehat{Z}_{\mathrm{A}}\cos(\widehat{k}_{\mathrm{A}}d) - i\widehat{Z}_{\mathrm{F}}\sin(\widehat{k}_{\mathrm{A}}d)}\,\frac{\widehat{Z}_{\mathrm{F}}Q}{2}\,\mathrm{e}^{i\widehat{k}_{\mathrm{F}}a}.$$

Using now (19) and the inverse Fourier transform, we have

$$P_1(\boldsymbol{x}) = \frac{i\omega\rho_{\mathrm{F}}Q}{4\pi}\,\frac{\mathrm{e}^{ik_{\mathrm{F}}|\boldsymbol{x}-\boldsymbol{a}|}}{|\boldsymbol{x}-\boldsymbol{a}|} + P_1^R(\boldsymbol{x}),$$

where

$$P_1^R(\boldsymbol{x}) = \frac{1}{(2\pi)^2}\int_{-\infty}^{+\infty}\int_{-\infty}^{+\infty}\widehat{R}_1(\widehat{x}_1,\widehat{x}_2)\,\mathrm{e}^{i\widehat{k}_{\mathrm{F}}x_3}\,\mathrm{e}^{i\widehat{x}_1x_1}\,\mathrm{e}^{i\widehat{x}_2x_2}\,d\widehat{x}_1\,d\widehat{x}_2.$$

Since $\widehat{R}_1$ depends on $\widehat{x}_1$ and $\widehat{x}_2$ only through $\widehat{r}$, by using the Hankel transform[24] we can rewrite the pressure field in Ω_{F} as follows:

$$P_1(\boldsymbol{x}) = \frac{i\omega\rho_{\mathrm{F}}Q}{4\pi}\,\frac{\mathrm{e}^{ik_{\mathrm{F}}|\boldsymbol{x}-\boldsymbol{a}|}}{|\boldsymbol{x}-\boldsymbol{a}|} + \frac{1}{2\pi}\int_0^{+\infty}\widehat{R}_1(\widehat{r})\,\mathrm{e}^{i\widehat{k}_{\mathrm{F}}x_3}\,\mathrm{J}_0\left(\widehat{r}\sqrt{x_1^2+x_2^2}\right)\widehat{r}\,d\widehat{r}, \quad (21)$$

where J_0 denotes the Bessel function of first kind and order zero.

The above integral can be computed exactly only if the geometry is very simple. Otherwise, some quadrature rule has to be used. In such case, numerical problems should be expected because the function $\widehat{R}_1(\widehat{r})$ has a singularity at $\widehat{r} = k_{\mathrm{F}}$.

By applying similar techniques to the wall impedance model, we can also write explicitly the solution of (9)-(11) as follows:

$$P_2(\boldsymbol{x}) = \frac{i\omega\rho_{\mathrm{F}}Q}{4\pi}\,\frac{\mathrm{e}^{ik_{\mathrm{F}}|\boldsymbol{x}-\boldsymbol{a}|}}{|\boldsymbol{x}-\boldsymbol{a}|} + \frac{1}{2\pi}\int_0^{+\infty}\widehat{R}_2(\widehat{r})\,\mathrm{e}^{i\widehat{k}_{\mathrm{F}}x_3}\,\mathrm{J}_0\left(\widehat{r}\sqrt{x_1^2+x_2^2}\right)\widehat{r}\,d\widehat{r}, \quad (22)$$

where $\widehat{R}_2$ is given by

$$\widehat{R}_2 = \mathrm{e}^{-2i\widehat{k}_{\mathrm{F}}d}\,\frac{Z+\widehat{Z}_{\mathrm{F}}}{Z-\widehat{Z}_{\mathrm{F}}}\,\frac{\widehat{Z}_{\mathrm{F}}Q}{2}\,\mathrm{e}^{i\widehat{k}_{\mathrm{F}}a}.$$

Our next goal is to compare the solutions (21) and (22) when the wall impedance Z is taken according to (14).

We have used the same values for the physical and geometrical parameters as in the previous test. The integrals in (21) and (22) have been computed by using recursive adaptive Lobatto quadrature[25] with a tolerance error of 10^{-8} and truncating the integration domain at a distance 10^{-7} to the singular point $\widehat{r} = k_{\mathrm{F}}$.

We have computed P_1 and P_2 at the same points as in the previous test for different frequencies. The real parts of the results are shown in Fig. 7, where an excellent agreement between both models can be clearly observed again for a wide range of frequencies. Once more, the agreement is so good that it is very hard to distinguish the curves corresponding to each model.

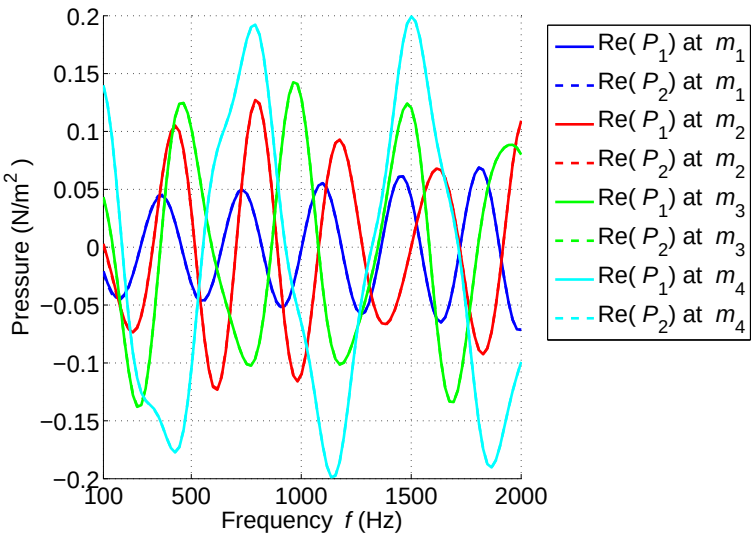

Figure 7: Spherical waves. Real part of the pressure fields at different points lying on the x_3-axis.

We have also computed P_1 and P_2 at points $\boldsymbol{m}_5$, $\boldsymbol{m}_6$, $\boldsymbol{m}_7$ and $\boldsymbol{m}_8$, not lying on the x_3-axis (see Fig. 4) for different frequencies. The real parts of the results, are shown in Fig. 8. Once more, for each of the observation points, the curves corresponding to each model almost coincide because of the excellent agreement.

Finally, Fig. 9 shows the relative difference between both solutions, $|P_1 - P_2| \,/\, |P_{\mathrm{inc}}|$, at points $\boldsymbol{m}_3$, $\boldsymbol{m}_4$ and $\boldsymbol{m}_8$, for a couple of frequencies and a range of values of the thickness. The incidence pressure P_{inc} is now the first term in the right hand sides of Eq. (21) and (22), namely,

$$P_{\mathrm{inc}} = \frac{i\omega\rho_{\mathrm{F}} Q}{4\pi} \, \frac{\mathrm{e}^{ik_{\mathrm{F}}|\boldsymbol{x}-\boldsymbol{a}|}}{|\boldsymbol{x}-\boldsymbol{a}|}. \tag{23}$$

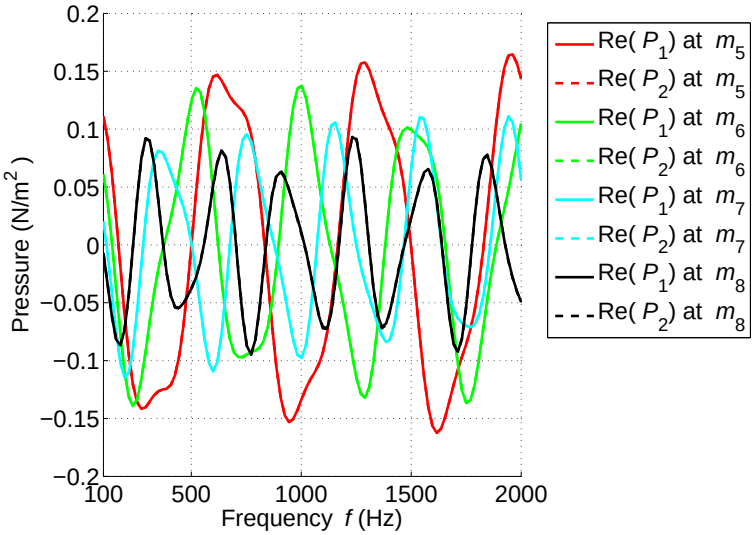

Figure 8: Spherical waves. Real part of the pressure fields at different points lying on the line $x_3 = 0.55$.

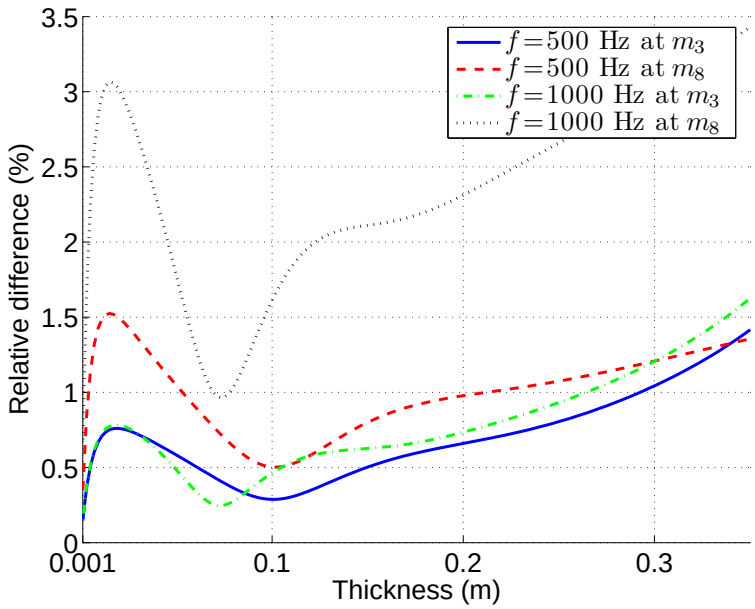

Figure 9: Spherical waves. $|P_1 - P_2| \,/\, |P_{\text{inc}}|$ versus thickness of the porous layer.

It can be checked that the agreement between both models gets worse for large values of d. Anyway, for rather thick porous media layers and moderate values of the frequency, the agreement is excellent, the relative difference remaining smaller than 3%.

4 Curved wall

In the previous section, we have solved analytically the Allard-Champoux and the wall impedance models in two particular cases, taking advantage of the special geometric configuration of the domains (planar interfaces and unbounded fluid and porous media). However, in real problems, the obstacle and the porous layer are bounded and have arbitrary shapes, usually with non-planar boundaries.

In this framework, we are going to focus our attention on the comparison of both models in the case of non-planar geometries. Since in such case it is not possible to compute the exact solutions using analytical techniques, it is necessary to introduce a computational method. This is the aim of the rest of the paper.

From a computational point of view, we have to deal with two main difficulties:

- the fluid domain is unbounded,
- the thickness of the porous layer is much smaller than the other dimensions.

We overcome the first difficulty by using the Perfectly Matched Layer technique[18] with optimal choice of the absorbing function,[26] as described in Subsection 4.1 below.

The second difficulty becomes relevant when we try to solve numerically problem (1)-(7) in three-dimensional domains by applying a finite-element method. Indeed, because of the different scales in the dimensions of the porous layer, it is necessary to use meshes with a large number of degrees of freedom to obtain a good accuracy of the results, which in turn implies to solve large linear systems of equations.

For simplicity, we restrict our analysis to axisymmetric problems. Let (r, θ, φ) denote the standard spherical coordinates of a point $\boldsymbol{x} \in \mathbb{R}^3$ (see Fig. 10) and $\{\boldsymbol{e}_r, \boldsymbol{e}_\theta, \boldsymbol{e}_\varphi\}$ the canonical basis associated to this system of coordinates. We consider problems such that the porous and fluid domains as well as the external source are independent of the azimuthal angle φ. In such case Eq. (1)-(7) and (9)-(11) can be rewritten in terms of r and θ, and, hence, reduced to two dimensions.

4.1 The Perfectly Matched Layer

We introduce a PML technique in spherical coordinates[27] to truncate the unbounded fluid domain.

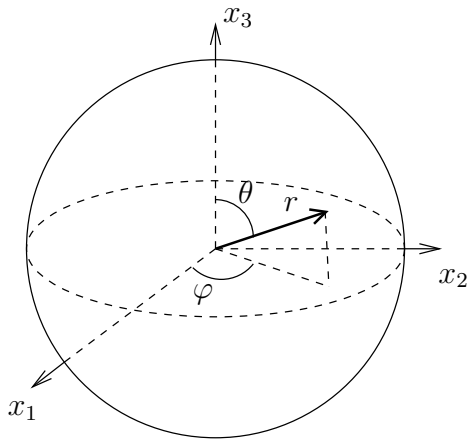

$$x_1 = r\sin\theta\cos\varphi,$$
$$x_2 = r\sin\theta\sin\varphi,$$
$$x_3 = r\cos\theta.$$

Figure 10: Spherical coordinates.

For this purpose, we surround the domain of interest (i.e., the part of the domain where we want to compute the pressure field) with a spherical PML. We consider a ball of radius R containing the domain of interest, the porous layer and the scatterer. The PML occupies the annular domain $\widetilde{\Omega}_{\mathrm{F}} = \{\boldsymbol{x} \in \Omega_{\mathrm{F}} : R < |\boldsymbol{x}| < R^\star\}$ and we denote by Γ_{M} and Γ_{D} the spherical surfaces of radius R and $R^\star$, respectively, so that the boundary of $\widetilde{\Omega}_{\mathrm{F}}$ is $\Gamma_{\mathrm{M}} \cup \Gamma_{\mathrm{D}}$, as shown in Fig. 11 (left). Notice that $\boldsymbol{e}_r$ is a unit normal vector for both surfaces.

From now on, we make an abuse of notation: we denote with the same names the original three-dimensional domains and the corresponding two-dimensional projections, namely,

$$\Omega_{\mathrm{F}} = \{(r,\theta) : \boldsymbol{x} = (r,\theta,\varphi) \in \Omega_{\mathrm{F}}\}, \qquad \Gamma_{\mathrm{I}} = \{(r,\theta) : \boldsymbol{x} = (r,\theta,\varphi) \in \Gamma_{\mathrm{I}}\}, \qquad \text{etc.}$$

See Fig. 11 for a better understanding of this notation.

Problems (1)-(7) and (9)-(11) are respectively written in this two-dimensional spherical coordinates setting as follows, where $\widetilde{P}_j$ $(j = 1, 2)$ denote the pressure

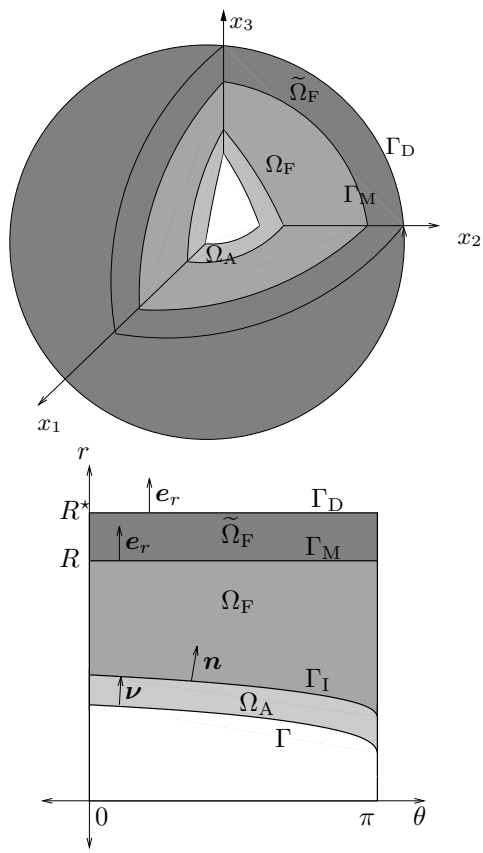

Figure 11: Original axisymmetric (cut) domains and spherical coordinates domains.

fields in $\widetilde{\Omega}_{\mathrm{F}}$:

$$\left\{\begin{array}{rl}
\dfrac{1}{\rho_{\mathrm{F}}}\,\mathrm{div}\,(\boldsymbol{\nabla} P_1) + \dfrac{\omega^2}{\mu_{\mathrm{F}}} P_1 = F & \text{in } \Omega_{\mathrm{F}}, \\
\dfrac{1}{\rho_{\mathrm{A}}}\,\mathrm{div}\,(\boldsymbol{\nabla} P_{\mathrm{A}}) + \dfrac{\omega^2}{\mu_{\mathrm{A}}} P_{\mathrm{A}} = 0 & \text{in } \Omega_{\mathrm{A}}, \\
\dfrac{1}{\rho_{\mathrm{F}}}\,\widetilde{\mathrm{div}}\left(\widetilde{\boldsymbol{\nabla}} \widetilde{P}_1\right) + \dfrac{\omega^2}{\mu_{\mathrm{F}}} \widetilde{P}_1 = 0 & \text{in } \widetilde{\Omega}_{\mathrm{F}}, \\
P_1 = P_{\mathrm{A}} & \text{on } \Gamma_{\mathrm{I}}, \\
\dfrac{1}{\rho_{\mathrm{F}}} \dfrac{\partial P_1}{\partial \boldsymbol{n}} = \dfrac{1}{\rho_{\mathrm{A}}} \dfrac{\partial P_{\mathrm{A}}}{\partial \boldsymbol{n}} & \text{on } \Gamma_{\mathrm{I}}, \\
\dfrac{1}{\rho_{\mathrm{A}}} \dfrac{\partial P_{\mathrm{A}}}{\partial \boldsymbol{\nu}} = 0 & \text{on } \Gamma, \\
P_1 = \widetilde{P}_1 & \text{on } \Gamma_{\mathrm{M}}, \\
\dfrac{1}{\rho_{\mathrm{F}}} \dfrac{\partial P_1}{\partial r} = \dfrac{1}{\rho_{\mathrm{F}}} \widetilde{\boldsymbol{\nabla}} \widetilde{P}_1 \cdot \boldsymbol{e}_r & \text{on } \Gamma_{\mathrm{M}}, \\
\widetilde{P}_1 = 0 & \text{on } \Gamma_{\mathrm{D}}.
\end{array}\right. \tag{24}$$

$$
\begin{cases}
\dfrac{1}{\rho_{\mathrm{F}}}\operatorname{div}(\boldsymbol{\nabla} P_2) + \dfrac{\omega^2}{\mu_{\mathrm{F}}} P_2 = F & \text{in } \Omega_{\mathrm{F}}, \\
\dfrac{1}{\rho_{\mathrm{F}}}\widetilde{\operatorname{div}}\left(\widetilde{\boldsymbol{\nabla}}\widetilde{P}_2\right) + \dfrac{\omega^2}{\mu_{\mathrm{F}}}\widetilde{P}_2 = 0 & \text{in } \widetilde{\Omega}_{\mathrm{F}}, \\
P_2 - \dfrac{Z}{i\omega\rho_{\mathrm{F}}}\dfrac{\partial P_2}{\partial \boldsymbol{\nu}} = 0 & \text{on } \Gamma_{\mathrm{I}}, \\
P_2 = \widetilde{P}_2 & \text{on } \Gamma_{\mathrm{M}}, \\
\dfrac{1}{\rho_{\mathrm{F}}}\dfrac{\partial P_2}{\partial r} = \dfrac{1}{\rho_{\mathrm{F}}}\widetilde{\boldsymbol{\nabla}}\widetilde{P}_2 \cdot \boldsymbol{e}_r & \text{on } \Gamma_{\mathrm{M}}, \\
\widetilde{P}_2 = 0 & \text{on } \Gamma_{\mathrm{D}}.
\end{cases}
\tag{25}
$$

In the previous systems, the differential operators div and $\boldsymbol{\nabla}$ are, respectively, the divergence and gradient differential operators in spherical coordinates for axisymmetric problems (i.e., with vanishing partial derivatives with respect to φ):

$$
\begin{aligned}
\boldsymbol{\nabla} Q =& \frac{\partial Q}{\partial r}\boldsymbol{e}_r + \frac{1}{r}\frac{\partial Q}{\partial \theta}\boldsymbol{e}_\theta, \\
\operatorname{div}\boldsymbol{w} =& \frac{1}{r^2}\frac{\partial}{\partial r}(r^2 w_r) + \frac{1}{r\sin\theta}\frac{\partial}{\partial\theta}(\sin\theta w_\theta),
\end{aligned}
$$

where $\boldsymbol{w} = w_r\boldsymbol{e}_r + w_\theta\boldsymbol{e}_\theta$. On the other hand, $\widetilde{\operatorname{div}}$ and $\widetilde{\boldsymbol{\nabla}}$ are the differential operators associated to the specific complex change of coordinates typical of the PML technique:[28]

$$
\begin{aligned}
\widetilde{\boldsymbol{\nabla}} Q =& \frac{1}{\gamma_r}\frac{\partial Q}{\partial r}\boldsymbol{e}_r + \frac{1}{r\widehat{\gamma}_r}\frac{\partial Q}{\partial \theta}\boldsymbol{e}_\theta, \\
\widetilde{\operatorname{div}}\,\boldsymbol{w} =& \frac{1}{r^2\gamma_r\widehat{\gamma}_r^2}\frac{\partial}{\partial r}(r^2\widehat{\gamma}_r^2 w_r) + \frac{1}{r\widehat{\gamma}_r\sin\theta}\frac{\partial}{\partial\theta}(\sin\theta w_\theta),
\end{aligned}
$$

where

$$
\gamma_r(r) = 1 + \frac{i}{\omega}\sigma_r(r) \qquad \text{and} \qquad \widehat{\gamma}_r(r) = 1 + \frac{i}{r\omega}\int_R^r \sigma_r(s)\,ds, \qquad R < r < R^\star,
$$

with σ_r being the variable absorption coefficient in the PML.

The typical choices for σ_r are constant, linear or parabolic functions.[18, 29] Instead, we use a non-integrable absorbing function σ_r, which allows us to recover the exact solution of the original scattering problem in the domain of interest.[26] In particular we use

$$
\sigma_r(s) = \frac{c_{\mathrm{F}}}{R^\star - s}, \qquad R < r < R^\star, \tag{26}
$$

which has been shown to be an optimal choice.[20]

4.2 Finite-element discretization

In this section we introduce a standard finite-element method to solve numerically the variational formulations of problems (24) and (25).

Consider a quadrangular mesh of domains $\Omega_{\rm A}$, $\Omega_{\rm F}$ and $\widetilde{\Omega}_{\rm F}$, matching on the common interfaces, $\Gamma_{\rm I}$ and $\Gamma_{\rm M}$, respectively (see Fig. 12).

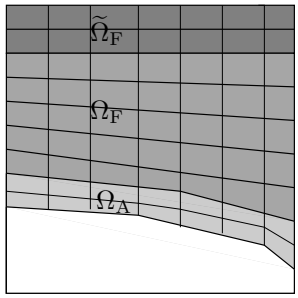

Figure 12: Quadrangular finite elements for the domains in spherical coordinates.

Regarding problem (24), we will compute approximations $P_{{\rm A}h}$, P_{1h} and $\widetilde{P}_{1h}$ of the pressure amplitude in $\Omega_{\rm A}$, $\Omega_{\rm F}$ and $\widetilde{\Omega}_{\rm F}$, respectively, by using continuous piecewise bilinear quadrangular finite elements. The degrees of freedom defining the finite-element solution are the values of $P_{{\rm A}h}$, P_{1h} and $\widetilde{P}_{1h}$ at the vertices of the elements. Notice that, because of the transmission conditions, $P_{{\rm A}h} = P_{1h}$ on $\Gamma_{\rm I}$ and $P_{1h} = \widetilde{P}_{1h}$ on $\Gamma_{\rm M}$, and, hence, the values of these functions must coincide at the vertices on the interfaces. Moreover, because of the boundary condition, $P_{1h} = 0$ on $\Gamma_{\rm D}$.

Standard arguments lead to the following discrete problem from the variational formulation of problem (24):

$$\int_{\Omega_{\rm F}} \left(\boldsymbol{\nabla} P_{1h} \cdot \boldsymbol{\nabla} \overline{Q}_h - k_{\rm F}^2 P_{1h} \overline{Q}_h\right) dS + \int_{\Omega_{\rm A}} \left(\boldsymbol{\nabla} P_{{\rm A}h} \cdot \boldsymbol{\nabla} \overline{Q}_h - k_{\rm A}^2 P_{{\rm A}h} \overline{Q}_h\right) dS$$
$$+ \int_{\widetilde{\Omega}_{\rm F}} \left(\frac{\widehat{\gamma}_r^2}{\gamma_r} \frac{\partial \widetilde{P}_{1h}}{\partial r} \frac{\partial \overline{Q}_h}{\partial r} + \frac{\gamma_r}{r^2} \frac{\partial \widetilde{P}_{1h}}{\partial \theta} \frac{\partial \overline{Q}_h}{\partial \theta} \, dS - k_{\rm F}^2 \widehat{\gamma}_r^2 \gamma_r \widetilde{P}_{1h} \overline{Q}_h \right) dS = \int_{\Omega_{\rm F}} \rho_{\rm F} F \overline{Q}_h \, dS,$$

for all discrete test pressure field Q_h in the corresponding finite-element space. Recall that the surface element $dS = r \sin\theta \, dr \, d\theta$. Let us remark that the integrals in the above problem are well defined, in spite of the non-integrable character of the absorbing function (26).[20]

Analogously, the following is the discrete problem corresponding to (25):

$$\int_{\Omega_{\rm F}} \left(\boldsymbol{\nabla} P_{2h} \cdot \boldsymbol{\nabla} \overline{Q}_h - k_{\rm F}^2 P_{2h} \overline{Q}_h\right) dS - \int_{\Gamma_{\rm I}} \frac{i\omega\rho_{\rm F}}{Z} P_{2h} \overline{Q}_h \, dL$$
$$+ \int_{\widetilde{\Omega}_{\rm F}} \left(\frac{\widehat{\gamma}_r^2}{\gamma_r} \frac{\partial \widetilde{P}_{2h}}{\partial r} \frac{\partial \overline{Q}_h}{\partial r} + \frac{\gamma_r}{r^2} \frac{\partial \widetilde{P}_{2h}}{\partial \theta} \frac{\partial \overline{Q}_h}{\partial \theta} - k_{\rm F}^2 \widehat{\gamma}_r^2 \gamma_r \widetilde{P}_{2h} \overline{Q}_h \right) dS = \int_{\Omega_{\rm F}} \rho_{\rm F} F \overline{Q}_h \, dS,$$

for all discrete test pressure field Q_h in the corresponding finite-element space; dL stands for the arc-length element. Notice that, once more, $P_{2h} = \widetilde{P}_{2h}$ on Γ_{M} and $P_{2h} = 0$ on Γ_{D}.

4.3 Verification of the numerical methods

In this section we verify the numerical methods that we have introduced in Section 4.2; namely, the PML model with a singular absorbing function and the finite element methods in spherical coordinates to approximate each model: Allard-Champoux and wall impedance. With this purpose, we have solved two simple problems, one for each model, both of them with known analytical solutions.

4.3.1 Verification of the numerical method for the Allard-Champoux model

In the first test, we check the accuracy of the numerical approximation of the Allard-Champoux model. Let Ω be a sphere centered at the origin of coordinates (see Fig. 13). We consider problem (1)-(7) with $F = 0$ and Eq. (5) substituted by the following one: $\dfrac{\partial P_{\mathrm{A}}}{\partial \boldsymbol{\nu}} = 1$ on Γ. In this case, the solution is a superposition of two spherical waves:

$$P_{\mathrm{A}}(\boldsymbol{x}) = A_{\mathrm{A}} \frac{\mathrm{e}^{ik_{\mathrm{A}} r}}{r} + B_{\mathrm{A}} \frac{\mathrm{e}^{-ik_{\mathrm{A}} r}}{r},$$
$$P_1(\boldsymbol{x}) = A_1 \frac{\mathrm{e}^{ik_{\mathrm{F}} r}}{r} + B_1 \frac{\mathrm{e}^{-ik_{\mathrm{F}} r}}{r}.$$

The pairs of complex constants A_{A}, A_1 and B_{A}, B_1 are, respectively, the amplitudes of the ingoing and outgoing spherical waves in the porous media and the fluid. They are determined by the transmission and boundary conditions of the problem.

We have taken an inner sphere of radius $R_0 = 0.5\,\mathrm{m}$, $R = 1.6\,\mathrm{m}$ and $R^\star = 1.8\,\mathrm{m}$. We have used the same values for the physical parameters as in Section 3: $\rho_{\mathrm{F}} = 1.2\,\mathrm{kg/m^3}$, $c_{\mathrm{F}} = 343\,\mathrm{m/s}$, $\mathrm{Pr} = 0.702$, $\gamma = 1.4$, $\sigma = 20000$ rays mks, $P_0 = 101320\,\mathrm{N/m^2}$ and $d = 0.05\,\mathrm{m}$.

We have used uniform refinements of the mesh shown in Fig. 15. The number N of elements through the thickness of the PML is used to label each mesh.

We compare in Fig. 16 the exact and the computed solution of the Allard-Champoux model along the x_3-axis, for a frequency $f = 1000\,\mathrm{Hz}$. The computed solution was obtained with the mesh corresponding to $N = 12$, which has 5145 degrees of freedom. The solution is plotted in the physical domain and in the PML.

To measure the accuracy of the numerical solution we have computed the

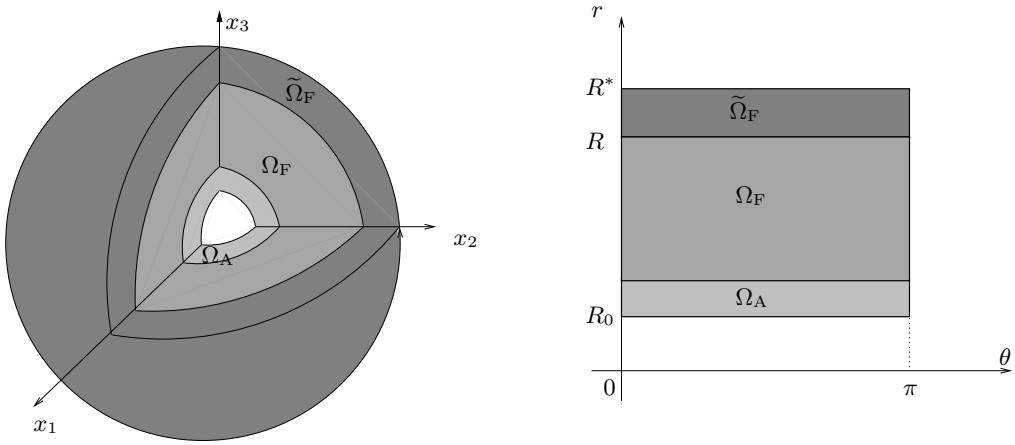

Figure 13: Three-dimensional cut of the spherical geometry and spherical coordinates domains.

relative error in L^2-norm:

$$\frac{\left(\int_{\Omega_{\mathrm{F}}} |P_{1h} - P_1|^2 \, dS\right)^{1/2}}{\left(\int_{\Omega_{\mathrm{F}}} |P_1|^2 \, dS\right)^{1/2}}.$$

We report in Fig. 17 the error curves (log-log plot of errors versus degrees of freedom) for a couple of frequencies. For instance, in the case of Fig. 16, the relative error is 18.15%.

Fig. 17 allow us to asses the order of convergence of the method. It can be seen that a quadratic order of convergence is achieved in all cases. Let us recall that this is the optimal order for the finite elements we have used.

4.3.2 Verification of the numerical method for the wall impedance model

In the second test, we check the accuracy of the numerical approximation of the wall impedance model. We use the same values for the physical and geometrical parameters as in the previous test. We consider now problem (9)-(11) with $F = 0$ and the boundary condition $P_2 = \dfrac{Z}{i\omega\rho_{\mathrm{F}}} \dfrac{\partial P_2}{\partial \boldsymbol{n}} + 1$ on Γ_{I}, instead of Eq. (10). The solution is a spherical wave

$$P_2(\boldsymbol{x}) = A_2 \frac{\mathrm{e}^{ik_{\mathrm{F}} r}}{r} + B_2 \frac{\mathrm{e}^{-ik_{\mathrm{F}} r}}{r},$$

whose complex coefficients, A_2 and B_2, can be explicitly determined from the boundary conditions of the problem.

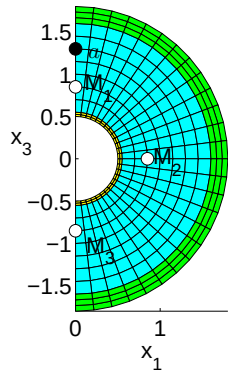

Figure 14: Coarse mesh for Allard-Champoux model in Cartesian coordinates ($N = 3$).

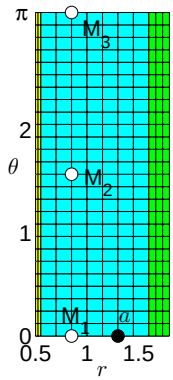

Figure 15: Coarse mesh for Allard-Champoux model in spherical coordinates ($N = 3$).

We have used the same meshes as in the previous test, excluding the elements in Ω_{A}.

We compare in Fig. 18 the exact and the computed solution of the wall impedance model along the x_3-axis, for a frequency $f = 1000\,\mathrm{Hz}$. The computed solution was obtained with the mesh corresponding to $N = 12$ (5145 degrees of freedom).

Fig. 19 shows the error curves for a couple of frequencies. For instance, in the case of Fig. 18, the relative error is 9.83%. The order of convergence is again optimal (quadratic).

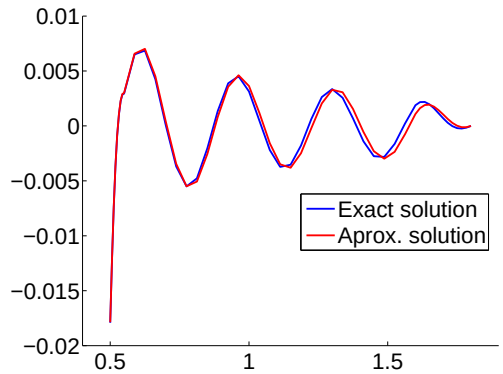

Figure 16: Real part of the pressure field computed with Allard-Champoux model. Mesh: $N = 12$ (5145 degrees of freedom); frequency: $f = 1000\,\mathrm{Hz}$.

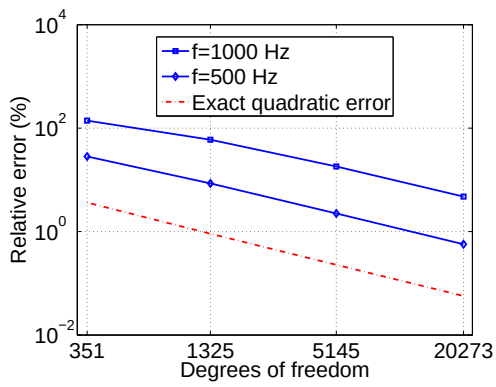

Figure 17: Error curve for Allard-Champoux model.

4.4 Numerical validation of the wall impedance model for non-planar geometries

In this section we validate the wall impedance model by means of a test involving non-planar geometries. With this purpose, we compare the results of this model with those obtained with Allard-Champoux model. We will show that the geometry and the data of the problem are essential factors which can affect the agreement shown in Section 3.

We study the reflection of a spherical wave scattered by a non-concentric spherical obstacle. The solution of this problem has been broadly studied in the literature and an exact solution can be obtained via a series representation.[30, 31]

We have used the physical parameters and the geometry described in Sec-

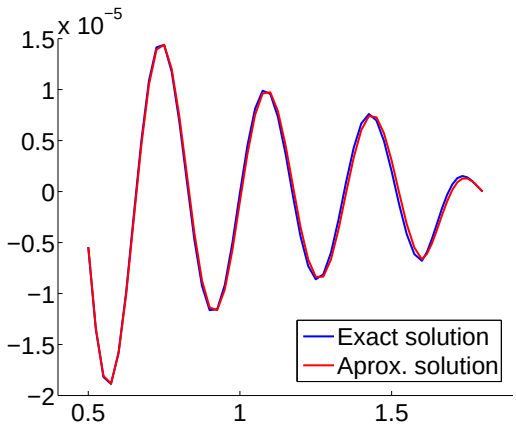

Figure 18: Real part of the pressure field computed with the wall impedance model. Mesh: $N = 12$ (5145 degrees of freedom); frequency: $f = 1000\,\mathrm{Hz}$.

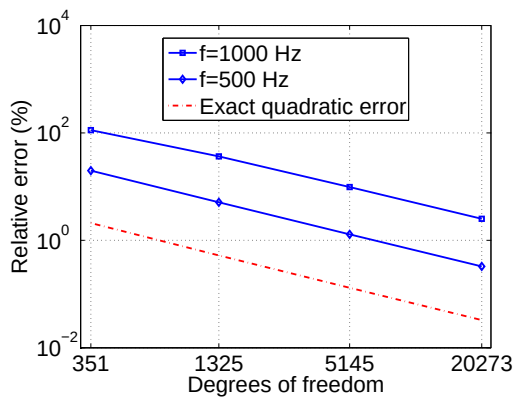

Figure 19: Error curves for wall impedance model.

tion 4.3. We have taken as external source a monopole with volume velocity $Q = 1\,\mathrm{m}^3/\mathrm{s}$ acting at the point $\boldsymbol{a} = (0, 0, a)$, with $a = 1.3\,\mathrm{m}$ (see Figs. 14 and 15).

Figs. 20 and 21 show the real parts of the pressure fields computed with each model on the mesh corresponding to $N = 12$, for a frequency $f = 500\,\mathrm{Hz}$ and a thickness of the porous layer $d = 0.05\,\mathrm{m}$. In all cases, the solution is plotted in the physical domain and in the PML. The pressure field has not been plotted around the monopole location to avoid scale distortions due to excessively large pressure values arising from the singularity.

We have checked the agreement between both models by comparing the values of the pressure field computed with each model at three points in the fluid

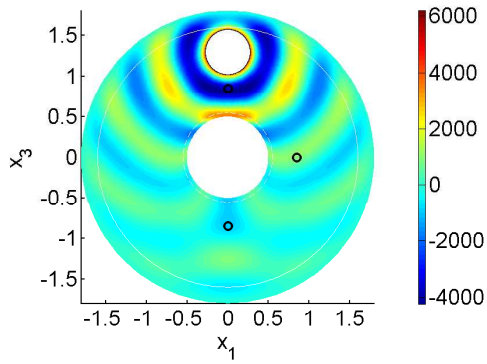

Figure 20: Real part of the pressure field computed with Allard-Champoux model. Mesh: $N = 12$; frequency: $f = 500\,\mathrm{Hz}$; thickness $d = 0.05\,\mathrm{m}$.

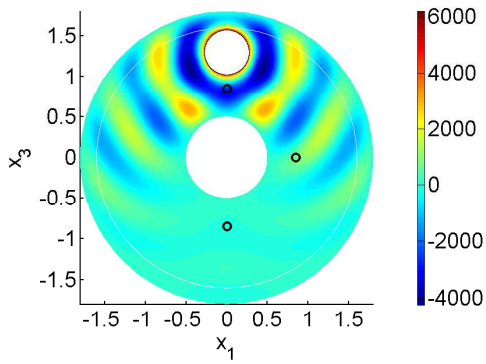

Figure 21: Real part of the pressure field computed with the wall impedance model. Mesh: $N = 12$; frequency: $f = 500\,\mathrm{Hz}$; thickness $d = 0.05\,\mathrm{m}$.

domain: $\boldsymbol{M}_1 = (0, 0, b)$, $\boldsymbol{M}_2 = (0, b, 0)$ and $\boldsymbol{M}_3 = (0, 0, -b)$, with $b = 0.85\,\mathrm{m}$ (see Figs. 14 and 15). For each of these points, we have plotted the relative difference between both models, $|P_{1h} - P_{2h}| \,/\, |P_{\mathrm{inc}}|$, versus the frequency. In this expression, P_{1h} and P_{2h} are the values computed with Allard-Champoux and the wall impedance model, respectively, whereas P_{inc} is the incidence pressure as given by Eq. (23), which is the standard for spherical waves. Figs. 22 and 23 shows these plots for two values of the thickness: $d = 0.05\,\mathrm{m}$ and $d = 0.2\,\mathrm{m}$, respectively.

We observe large differences between the solutions obtained with both models in many cases. For instance, the curves corresponding to points $\boldsymbol{M}_1$ and $\boldsymbol{M}_2$

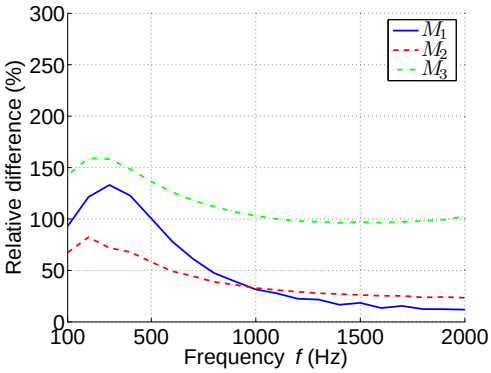

Figure 22: $|P_{1h} - P_{2h}| \,/\, |P_{\text{inc}}|$ versus frequency. Mesh: $N = 12$; thickness: $d = 0.05\,\text{m}$.

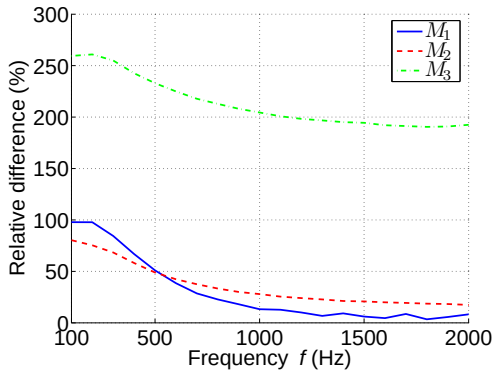

Figure 23: $|P_{1h} - P_{2h}| \,/\, |P_{\text{inc}}|$ versus frequency. Mesh: $N = 12$; thickness: $d = 0.2\,\text{m}$.

have peaks of around 100% at very low frequencies, although they show a reasonable agreement in the middle frequencies range. This behavior is essentially independent of the layer thickness.

Finally, we show in Figs. 24 and 25 the real parts of the pressure field computed with each model for a larger frequency, $f = 6000\,\text{Hz}$, and a thickness $d = 0.05\,\text{m}$. We have used in this case a very refined mesh corresponding to $N = 48$ in order to preserve the six elements per wave-length rule. A much better agreement can be observed in this case.

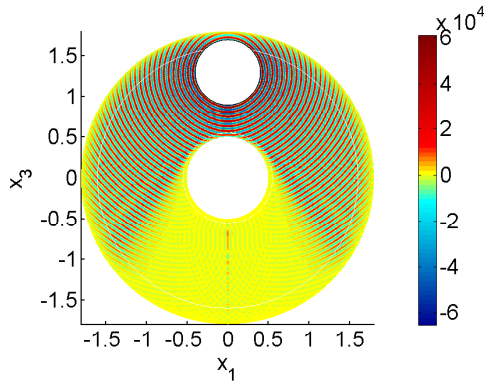

Figure 24: Real part of the pressure field computed with Allard-Champoux model. Mesh: $N = 48$; frequency: $f = 6000\,\mathrm{Hz}$; thickness: $d = 0.05\,\mathrm{m}$.

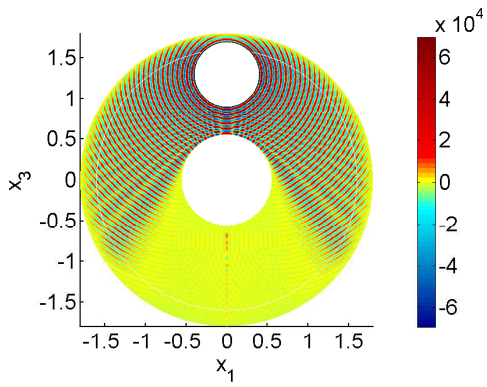

Figure 25: Real part of the pressure field computed with the wall impedance model. Mesh: $N = 48$; frequency: $f = 6000\,\mathrm{Hz}$; thickness: $d = 0.05\,\mathrm{m}$.

5 Conclusions

We have studied the agreement between two models for porous media in acoustic scattering problems: Allard-Champoux and a wall impedance model. We have shown that both provide almost identical results in planar geometries, even in the case of oblique incidence or spherical waves. This agreement holds for a wide range of frequencies, even for a non negligible thickness.

To be able to deal with non-planar geometries, we have introduced a finite-element method combined with an optimal bounded PML technique. We have

applied this numerical strategy to compute the pressure field scattered by a sphere. This numerical example has shown that the agreement between the model for non-planar geometries may be very poor.

¿From these results, we conclude that the simplified wall impedance model is suitable to model porous media in planar geometries, but not so reliable in more general cases.

References

[1] J.-F. Allard, *Propagation of Sound in Porous Media: Modelling Sound Absorbing Materials* (Elsevier, New York, 1993).

[2] M. A. Delany and E. N. Bazley, Acoustic properties of fibrous absorbent materials, *Appl. Acoust.* **3** (1970) 105–116.

[3] P. M. Morse and K. U. Ingard, *Theoretical Acoustics* (McGraw-Hill, New York, 1978).

[4] K. Attenborough, Acoustical characteristics of rigid fibrous absorbents and granular materials, *J. Acoust. Soc. Amer.* **73** (1983) 785–799.

[5] J.-F. Allard and Y. Champoux, New empirical equations for sound propagation in rigid frame fibrous materials, *J. Acoust. Soc. Amer.* **91** 6 (1992) 3346–3353.

[6] M. A. Biot, Theory of propagation of elastic waves in a fluid-saturated porous solid. I. Lower frequency range, *J. Acoust. Soc. Amer.* **28** (1956) 168–178.

[7] M. A. Biot, Theory of propagation of elastic waves in a fluid-saturated porous solid. II. Higher frequency range, *J. Acoust. Soc. Amer.* **28** (1956) 179–191.

[8] J. F. Allard, A. Aknine and C. Depollier, Acoustical properties of partially reticulated foams with high and medium flow resistance, *J. Acoust. Soc. Amer.* **79** (1986) 1734–1740.

[9] Th. Clopeau, J. L. Ferrín, R. P. Gilbert and A. Mikelić, Homogenizing the acoustic properties of the seabed II, *Math. Comput. Modelling*, **33** (2001) 821–841.

[10] A. Bermúdez, J. L. Ferrín and A. Prieto, Finite element solution of new displacement/pressure poroelastic models in acoustics, *Comput. Methods Appl. Mech. Eng.* **195** (2006) 1914–1932

[11] L. L. Beranek and I. L. Vér, *Noise and Vibration Control Engineering: Principles and Applications* (John Wiley & Sons, New York, 1992).

[12] V. Easwaran, W. Lauriks and J. P. Coyette, Displacement-based finite element method for guided wave propagation problems: application to poroelastic media, *J. Acoust. Soc. Amer.* **100** (1996) 2989–3002.

[13] R. Panneton and N. Atalla, An efficient finite element scheme for solving the three-dimensional poroelasticity problem in acoustics, *J. Acoust. Soc. Amer.* **101** (1997) 3287–3298.

[14] A. Bermúdez, J. L. Ferrín and A. Prieto, A finite element solution of acoustic propagation in rigid porous media, *Internat. J. Numer. Meth. Eng.* **62** (2005) 1295–1314.

[15] B. Engquist and A. Majda, Absorbing boundary conditions for the numerical simulation of waves, *Math. Comp.* **31** (1977) 629–651.

[16] F. Ihlenburg, *Finite Element of Analysis of Acoustical Scattering* (Springer-Verlag, New York, 1998).

[17] R. J. Astley, Infinite elements for wave problems: A review of current formulations and an assessment of accuracy, *Internat. J. Numer. Methods Eng.* **49** (2000) 951–976.

[18] J. P. Berenger, A perfectly matched layer for the absorption of electromagnetic waves, *J. Comput. Phys.* **114** (1994) 185–200.

[19] F. Collino and P. Monk, Optimizing the perfectly matched layer, *Comput. Methods Appl. Mech. Eng.* **164** (1998) 157–171.

[20] A. Bermúdez, L. Hervella-Nieto, A. Prieto and R. Rodríguez, An optimal perfectly matched layer with unbounded absorbing function for time-harmonic acoustic scattering problems, *J. Comput. Phys.* (to appear).

[21] C. H. Wilcox, *Sound Propagation in Stratified Fluids* (Springer-Verlag, New York, 1984).

[22] L. M. Brekhovskikh and O. A. Godin, *Acoustics of Layered Media I: Plane and Quasi-Plane Waves* (Springer, Berlin, 1999).

[23] D. G. Crighton, *Modern Methods in Analytical Acoustics* (Springer-Verlag, London, 1992).

[24] R. Bracewell, *The Fourier Transform and Its Applications* (McGraw-Hill, New York, 1999).

[25] W. Gander and W. Gautschi, Adaptive quadrature – revisited, *BIT*, 40 (2000) 84–101.

[26] A. Bermúdez, L. M. Hervella-Nieto, A. Prieto and R. Rodríguez, An exact bounded PML for the Helmholtz equation, *C. R. Acad. Sci. Paris, Ser. I*, **339** (2004) 803–808.

[27] P. G. Petropoulus, Reflectionless sponge layers as absorbing boundary conditions for the numerical solution of Maxwell's equations in rectangular, cylindrical and spherical coordinates, *SIAM J. Appl. Math.* **60** (2000) 1037–1058.

[28] W. C. Chew and W. H. Weedom, PML 3D perfectly matched medium from modified Maxwell's equations with stretched coordinates, *Microwave Opt. Technol. Lett.* **7** (1994) 599–604.

[29] F. Collino and P. Monk, The perfectly matched layer in curvilinear coordinates, *SIAM J. Sci. Comput.* **19** (1998) 2061–2090.

[30] Y. Arnaoudov, G. Dassios and V. Kostopoulos, The soft and the hard coated sphere within a point source wave field, *J. Acoust. Soc. Amer.* **104** (1998) 1929–1942.

[31] P. J. Morris, Scattering of sound from a spatially distributed, spherically symmetric source by a sphere, *J. Acoust. Soc. Amer.* **98** (1995) 3536–3539.